

Full length article

Phase field calculations of Sn redistribution in GeSn/Si structure after pulsed laser irradiation

Jevgenijs Kaupužs^a, Pavels Onufrijevs^{a,*} , Patrik Ščajev^b , Hung Hsiang Cheng^c, Guo-En Chang^d, Yoshishige Tsuchiya^e

^a Institute of Technical Physics, Faculty of Natural Sciences and Technology, Riga Technical University, Paula Valdena Street 7, Riga LV-1048, Latvia

^b Institute of Photonics and Nanotechnology, Vilnius University, Sauletekio av. 3, Vilnius 10257, Lithuania

^c Center for Condensed Matter Sciences and Graduate Institute of Electronics Engineering, National Taiwan University, Taipei 106, Taiwan

^d Department of Mechanical Engineering, and Advanced Institute of Manufacturing with High-Tech Innovations (AIM-HI), National Chung Cheng University, Chiayi 621301, Taiwan

^e School of Electronics and Computer Sciences, University of Southampton, Highfield Campus, Southampton SO17 1BJ, United Kingdom



ARTICLE INFO

Keywords:

Phase field model
Segregation
Impurity redistribution
Rapid solidification
Laser heating
GeSn

ABSTRACT

An innovative phase field model has been considered to describe the impurity redistribution in a rapid solidification process. This model has been implemented for the description of a complex process in GeSn/Si structure, consisting of the laser heating of solid phase, melting and solidification process. It allowed us to calculate the Sn concentration profile after repeated laser pulses. A significant increase of the Sn concentration near the surface is observed due to the segregation effect accumulated over many laser pulses. The obtained results are in a qualitative agreement with the experimental data for Ge_{0.04}Sn_{0.96} layer irradiated with nanosecond laser pulses. The differences between these results and those obtained earlier by the molecular beam epitaxy method are discussed.

1. Introduction

GeSn alloys have been recently applied in photodetectors [1–3], lasers [4,5], and other devices as high-mobility transistors [6], thermoelectrics [7]. This alloy becomes a direct bandgap semiconductor when Sn content exceeds 6–8 % [8,9]. Technologically it is a difficult task to obtain high Sn content due to the segregation [10], therefore non-equilibrium laser processing methods have been recently applied for Sn content enhancement [11–13]. Effective solution of the segregation problem would allow direct-bandgap GeSn application in silicon-based photonics, which can be used in data communication and information processing in the 1–3 μm spectral range [14]. Therefore, the redistribution of impurities during a rapid thermal treatment of GeSn material, including its melting and recrystallization, would have a great practical importance in various technological processes. It is therefore also very important to develop appropriate mathematical models for the simulation of such processes. It is often convenient to have a model, which allows to describe two phases (solid and liquid) without an explicit treating of the phase boundaries. Here we refer to the known phase field approach. Historically, it has been first developed as an

efficient method for description of the crystallization and growth of dendrites from pure melt [15–18]. Later on, it has been also applied to the kinetics of phase interface and impurity redistribution between solid and liquid phases of a binary system [19–22].

The phase field approach has been extended to the problems of hydrodynamics, as well. In particular, a coupled Navier-Stokes Cahn-Hilliard phase field has been developed in [23]. It has been employed, e.g., for investigating fluid-structure interaction problems within a fully Eulerian framework, using a fully-monolithic, implicit finite element method in [24]. In [25], a thermodynamically consistent phase field model has been introduced to investigate the hydrodynamics of inextensible multicomponent vesicles in various fluid flows. A residual-based variational multiscale method for the solution of the Navier-Stokes equations, as well as the standard Galerkin finite element method have been used there.

This study introduces an innovative phase field model to simulate impurity redistribution during rapid solidification processes, including heat sources and impurity dynamics while maintaining the original formulations of [18] for phase and temperature fields. As a basic simplification and approximation, we neglect the influence of the

* Corresponding author.

E-mail address: pavels.onufrijevs@rtu.lv (P. Onufrijevs).

<https://doi.org/10.1016/j.optlastec.2025.113046>

Received 31 December 2024; Received in revised form 15 April 2025; Accepted 23 April 2025

Available online 28 April 2025

0030-3992/© 2025 The Authors. Published by Elsevier Ltd. This is an open access article under the CC BY license (<http://creativecommons.org/licenses/by/4.0/>).

impurity redistribution on the phase and the temperature fields. However, the effect of these fields on the migration of impurities is taken into account. Within this approximation, our model describes consistently the redistribution of impurities, taking into account the gradients of both these fields. It distinguishes our approach from the one proposed earlier in [19–22], where a different pre-assumption has been made, trying mutually link the phase field and the impurity concentration, however, neglecting the effect of temperature gradient on the migration of impurities (see Section 2.1 for details).

Our model incorporates a novel method for initialization of the solid–liquid interface and introduces new boundary conditions, distinguishing it from previous models. Applied to a GeSn/Si structure

subjected to laser processing, the model demonstrates qualitative agreement with experimental Sn concentration profiles, indicating its potential for further quantitative refinement.

Looking for an easy implementation of our model, we have used a simple explicit difference scheme in our calculations. Since we deal with a one-dimensional problem, there is no problem with reaching a satisfactory accuracy of the numerical solution. The stability and accuracy tests in our paper (Section 2.3) show that this difference scheme provides a reliable solution of the equations considered. Only some small influence of the spatial step size can be mentioned, which is not harmful for an approximate comparison with the experimental data. Certainly, more accurate solution of our model could be found by more complex

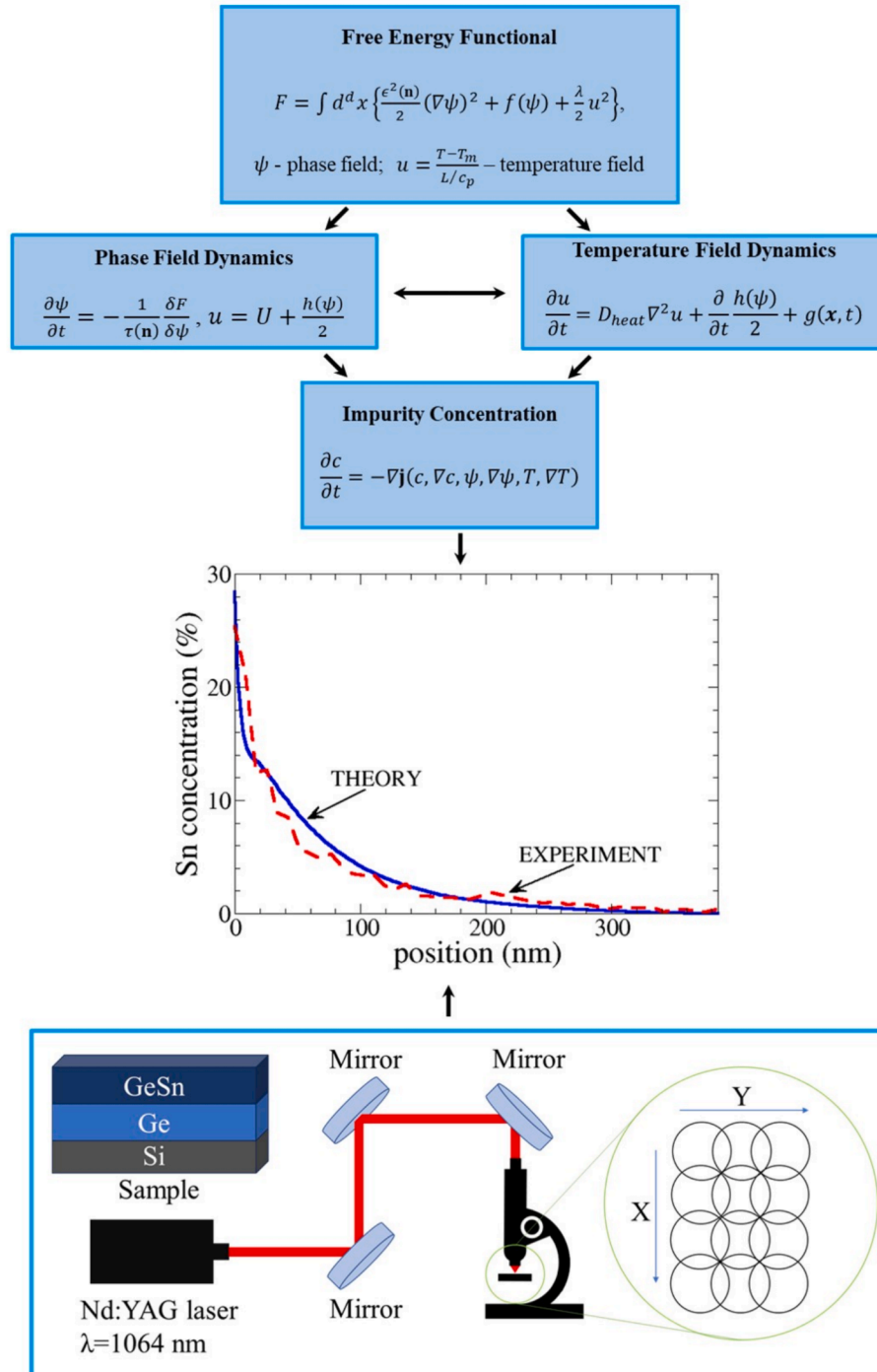


Fig. 1. A schematic illustration of the concept of our paper. The bottom picture shows GeSn irradiation setup working in a scanning mode [27].

and sophisticated finite element methods [24,25], potentially including also the machine learning algorithms [26]. At the current stage of development, our model itself still requires refinements for obtaining accurate quantitative results. It justifies the choice of a possibly simpler method of its solution.

The concept of our paper is illustrated in Fig. 1, where the connections between the phase field, the temperature field and the impurity concentration field in our model are shown schematically, resulting in the calculated impurity distribution after the laser processing. It is compared with the experimentally measured concentration profile [27]. The basic equations are also included here, which are further described in Section 2.

2. The phase field model

In the section 2.1 we describe the phase field model equations and further apply them for a GeSn/Si hetero-structure in the section 2.2.

2.1. The phase field model theory

In the phase field model, one considers the free energy functional [18].

In the phase field model, one considers the free energy functional [18]

$$F = \int d^d \mathbf{x} \left\{ \frac{\epsilon^2}{2} (\nabla \psi)^2 + f(\psi) + \frac{\lambda}{2} u^2 \right\} \quad (1)$$

where $\psi \in [-1, 1]$ is a continuously varying phase field depending on the coordinate \mathbf{x} in a d -dimensional space. It varies from -1 in the purely liquid phase to $+1$ in the purely solid phase, describing a continuous transformation between the two phases over a spatial region of the width $\sim \epsilon$. The parameter ϵ depends on the unit vector \mathbf{n} , which is oriented along the field gradient $\nabla \psi$, thus allowing to describe the anisotropy effects. The function $f(\psi)$ is the double-well potential

$$f(\psi) = -\frac{1}{2}\psi^2 + \frac{1}{4}\psi^4 \quad (2)$$

and

$$u = \frac{T - T_m}{L/c_p} \quad (3)$$

is the reduced temperature, where T is temperature, T_m is the melting temperature, L is the heat of fusion, and c_p is specific heat at a constant pressure. The parameter λ describes the coupling strength between the fields $\psi(\mathbf{x})$ and $u(\mathbf{x})$. One introduces the quantity $U = u - \frac{h(\psi)}{2}$, which is considered as an independent variable in the equations of motion. Here $h(\psi)$ is a function varying from $h(-1) = -1$ to $h(1) = 1$. We have chosen $h(\psi) = \frac{1}{2}\psi(3 - \psi^2)$, which has vanishing derivatives at $\psi = \pm 1$ and thus ensures that the functional (1) (where $u = U + h(\psi)/2$) has minimums at $\psi = \pm 1$ for a homogeneous $\psi(\mathbf{x})$. The equations of motion for ψ and U read [18]

$$\frac{\partial \psi}{\partial t} = -\frac{1}{\tau(\mathbf{n})} \frac{\delta F}{\delta \psi} \quad (4)$$

$$\frac{\partial U}{\partial t} = \frac{D_{heat}}{\lambda} \nabla^2 \frac{\delta F}{\delta U} \quad (5)$$

where $\tau(\mathbf{n})$ is the relaxation time of the solid-liquid interface and D_{heat} is the heat diffusivity. These equations ensure that F is the Liapunov functional, i.e., $\frac{\delta F}{\delta t} \leq 0$ holds, which means that F tends to its minimum. The corresponding equation for u reads [18]

$$\frac{\partial u}{\partial t} = D_{heat} \nabla^2 u + \frac{\partial h(\psi)}{\partial t} \quad (6)$$

It describes the variation of temperature field in the absence of external heat sources.

For our problem, we have added the source $g(\mathbf{x}, t)$ due to the heating by laser, i.e.,

$$\frac{\partial u}{\partial t} = D_{heat} \nabla^2 u + \frac{\partial h(\psi)}{\partial t} + g(\mathbf{x}, t) \quad (7)$$

and have solved the equations for ψ and u together with the continuity equation for impurity concentration $c(\mathbf{x}, t)$,

$$\frac{\partial c}{\partial t} = -\nabla \mathbf{j} \cdot (\mathbf{c}, \nabla \mathbf{c}, \psi, \nabla \psi, T, \nabla T) \quad (8)$$

where \mathbf{j} is the concentration flux. For a small concentration, it includes the diffusion term $-D\nabla c$ (the Fick's law), as well as drift terms $\propto c\nabla\psi$ and $\propto c\nabla T$. We have used the Einstein's relation $D = \mu k_B T$ between the diffusion coefficient D and the drift coefficient (mobility) μ , where k_B is the Boltzmann constant. The drift term with $\nabla\psi$ can be represented as $-c\mu\nabla E(\psi)$, where $E(\psi)$ is the potential energy of an impurity atom in the host material, which is varied from E_L in the liquid phase to E_S in the solid phase. An appropriate interpolation formula is $E(\psi) = p(\psi)E_S + (1-p(\psi))E_L + \Delta V q(\psi)$ with the function $p(\psi) = \frac{1}{2}(h(\psi) + 1)$, smoothly varying from $p(-1) = 0$ to $p(1) = 1$ and having the property $\frac{dp}{d\psi} = 0$ at $\psi = \pm 1$. The other function is $q(\psi) = (1 - \psi^2)^2$. It has the properties $q(\pm 1) = 0$, $q(0) = 1$ and $\frac{dq}{d\psi} = 0$ at $\psi = 0, \pm 1$. Hence, the term $\Delta V q(\psi)$ mimics the potential barrier of the height ΔV . This is the potential barrier created by the solid-liquid interface [19]. The choice of the functions $p(\psi)$ and $q(\psi)$ is not unique. We have chosen the simplest polynomial functions with the mentioned properties.

The drift term with ∇T is known to be $-c\mu Q^* \nabla T/T$ [28,29] for small c , where Q^* is the heat of transport. The diffusion and drift of impurity atoms can be considered as a stochastic process of jumping from one position to another discrete position. Any such a jump is possible only if the destination position is not occupied by another impurity atom. This effect has to be taken into account if the concentration c is not small. The Fick's law for the diffusion flux remains correct in this case, whereas the drift term is modified by the factor $1 - c$.

Noting that D and Q^* are dependent on ψ and T in general, these relations lead to the following expression for the flux \mathbf{j} :

$$\mathbf{j} = -D(T, \psi) \left(\nabla c + \left[\left(\frac{dp}{d\psi} \Delta \epsilon + \frac{dq}{d\psi} v \right) \nabla \psi + a(T, \psi) \nabla u \right] \frac{c(1-c)}{b+u} \right) \quad (9)$$

where $\Delta \epsilon = \frac{E_S - E_L}{k_B L/c_p}$, $v = \frac{\Delta V}{k_B L/c_p}$, $a = \frac{Q^*}{k_B T}$ and $b = \frac{T_m}{L/c_p}$ are dimensionless parameters.

Our equations represent a certain approximation, since we take into account the effect of the phase field and the temperature field on the flux of impurities, but do not consider the feedback. We also do not consider any interaction between the impurities except the exclusion effect, according to which two impurity atoms cannot occupy the same position.

Our approach is distinct from that one introduced in [19] and later used also in [20–22]. The basic idea in [19] is to obtain all equations of motion from the functional (1), where $f(\psi) \rightarrow f(\psi, c, T)$. The considered in that approach equation for the flux of c is partly consistent with (9), as it contains the diffusion term $\propto \nabla c$ and the drift term $\propto c(1-c)\nabla\psi$, but not the drift term with ∇T or ∇u contained in (9). Formally, one obtains the drift term of this kind from the equations of [19], i.e., from $\mathbf{j} = -M_2 c(1-c) \nabla \frac{\delta f}{\delta c}$ with f given by Eq. (36) in [19]. It appears to be proportional to $\ln c \nabla T$ at $c \rightarrow 0$, corresponding to a drift with divergent effective mobility in this limit. Hence, our phenomenological approach, where we have postulated a physically meaningful $\propto c(1-c)\nabla T$ form of this term, is preferable for the description of the effect of ∇T on the drift of impurities.

The equations, derived here, are suited for treating the two-phase system, but can also be used for a single phase, where $\nabla\psi \equiv 0$. More-

over, we have adopted them in Section 2.2 for the description of a complex process with only a solid phase at the beginning and melting process afterwards.

2.2. Model implementation for the GeSn structure

We have applied our equations to the modeling of Sn redistribution in GeSn material in a two-layer structure, consisting of a GeSn layer on Si substrate experimentally studied in [27]. Thus, we consider a one-dimensional problem. In this case, the equations of motion (4) and (7) reduce to

$$\frac{\partial \psi}{\partial t} = \frac{1}{\tau} \left\{ \epsilon^2 \frac{\partial^2 \psi}{\partial x^2} + \psi - \psi^3 - \frac{3}{4} \lambda u (1 - \psi^2) \right\} \quad (10)$$

$$\frac{\partial u}{\partial t} = D_{\text{heat}} \frac{\partial^2 u}{\partial x^2} + \frac{3}{4} (1 - \psi^2) \frac{\partial \psi}{\partial t} + g(x, t) \quad (11)$$

These are solved together with Eq. (8) for $c(x)$ in one dimension, where x is the distance from the surface of the structure. We consider the scenario, where only the GeSn layer with $x \in [0, l]$ can be melted, where $l = 385\text{nm}$. Thus, the phase field $\psi(x)$ refers only to this interval. The source in (11) has the form $g(x, t) = g_0 e^{-\alpha x}$ for $0 < t < t_{\text{pulse}}$ and $x \in [0, l]$, corresponding to the pulse of duration $t_{\text{pulse}} = 6\text{ns}$ and wavelength 1064nm (the first harmonic of Nd:YAG laser), for which Si is practically transparent. The absorption takes place in the GeSn layer only with the absorption coefficient α . We consider repeated laser pulses with the repetition frequency 10Hz . The heat accumulation from previous pulses is neglected, since the time interval between successive pulses is much longer than t_{pulse} .

The Sn concentration $c(x)$ within the GeSn layer $x \in [0, l]$ is considered. We use the interpolation formula

$$D(T, \psi) = p(\psi)D_s(T) + (1 - p(\psi))D_L(T) \quad (12)$$

for the diffusion coefficient $D(T, \psi)$, where $D_L(T)$ and $D_s(T)$ are the diffusion coefficients in the liquid and the solid phase, respectively. Since $D_s(T)$ is by many orders of magnitude smaller than $D_L(T)$, we have set $D_s(T) = 0$. Moreover, we have assumed that $D_L(T) = D_L$ is a constant. As one more simplification, we have neglected the effect of temperature gradient in (9), formally setting $a(T, \psi) = 0$. It is justified for $D_s(T) = 0$, since the redistribution of Sn atoms takes place only in the liquid phase with a relatively small temperature gradient in this case.

The numerical solution of Eqs. (10) and (11) has been performed in a standard way on a grid of x and t values, representing derivatives by finite differences. We use the spatial grid $x_i = i\Delta x$, where $i \geq 0$ is an integer number. The phase field ψ is defined within $i \in [0, N]$ with $x_N = l$, whereas u is defined within $i \in [0, M]$, where M is chosen large enough to simulate the case $x_M \rightarrow \infty$. Practically, x_M has to be chosen much larger than the heat diffusion length during the laser pulse and the solidification process after it. The second derivatives are expressed as $\left(\frac{\partial^2 \psi}{\partial x^2} \right)_{x=x_i} =$

$$\frac{\psi(x_{i+1}) - 2\psi(x_i) + \psi(x_{i-1}))}{(\Delta x)^2} \text{ for } i \in [1, N-1], \text{ and } \left(\frac{\partial^2 u}{\partial x^2} \right)_{x=x_i} = \frac{u(x_{i+1}) - 2u(x_i) + u(x_{i-1}))}{(\Delta x)^2} \text{ for } i \in [1, N-1] \cup [N+1, M-1].$$

The updates in time are performed by the Euler method, i.e., $\psi(x_i, t + \Delta t) = \psi(x_i, t) + \frac{\partial \psi(x_i, t)}{\partial t} \Delta t$, and similarly for $u(x_i, t + \Delta t)$. In this explicit central difference scheme, one needs also to know the values of ψ at $x = 0$ and $x = x_N$, the values of u at $x = 0, x_N, x_M$ (the boundary conditions), as well as the initial conditions. The boundary conditions for $u(x)$ were used, assuming the absence of any heat exchange with external media ($\nabla u = 0$ at $x = 0$ and $u = u_0 = \text{const}$ at $x \rightarrow \infty$), as well as the continuity of the heat flux $-\kappa \nabla T$ (where κ is the heat conductivity) at the GeSn/Si interface $x = x_N$. In the actual difference scheme, it means $u(0) = u(x_1)$, $u(x_N) = \frac{(\kappa_{\text{Si}}/\kappa_{\text{GeSn}})u(x_{N-1}) + u(x_{N-1})}{1 + (\kappa_{\text{Si}}/\kappa_{\text{GeSn}})}$ and $u(x_M) = u_0$. The initial condition $u(x_i, t) = u_0$ at $t = 0$ was used, corresponding to $T(x) = T_0 = 300\text{K}$.

In Eq. (8), the flux $j(x_i + \frac{\Delta x}{2})$ is calculated in the middle points between x_i and x_{i+1} for $i \in [0, N-1]$. For this purpose, the approximation $c(x_i + \frac{\Delta x}{2}) = \frac{1}{2}(c(x_i) + c(x_{i+1}))$ is used. Similarly, the quantities $D, \frac{dp}{d\psi}, \frac{dq}{d\psi}$ and u in the flux expression (9) are calculated by averaging over their values at $x = x_i$ and $x = x_{i+1}$. The gradients are approximated as $\nabla c = (c(x_{i+1}) - c(x_i))/\Delta x$ and $\nabla \psi = (\psi(x_{i+1}) - \psi(x_i))/\Delta x$. The divergence of flux is calculated as $\nabla j(x_i) = \frac{1}{\Delta x} (j(x_i + \frac{\Delta x}{2}) - j(x_i - \frac{\Delta x}{2}))$, setting $j(x_i - \frac{\Delta x}{2}) = j(x_N + \frac{\Delta x}{2}) = 0$ as the boundary conditions, implying zero flux out of the region $x \in [0, l]$. Inserting this into (8) and applying the Euler method for updating $c(x)$ in time, we obtain a conservative difference scheme, which conserves the total amount of impurity, or the quantity $\Delta x \sum_{i=0}^N c(x_i)$. We have set $c(x) = c_0(x)$ as the initial condition, where $c_0(x) = 0.04$ for $0 \leq x \leq 320\text{nm}$ and $c_0(x) = 0$ for $x > 320\text{nm}$.

A problem with the phase field $\psi(x)$ in Eqs. (10)-(11) is that there is no phase boundary at the beginning of the process, where $\psi(x) \equiv 1$, and it emerges spontaneously near the surface when the melting temperature is reached. The processes of melting and solidification has been simulated within the phase field approach, e.g., in [20], however, providing no details about the initialization of the solid-liquid interface. Routinely, one considers the situations, where this interface already exists. For the solid-liquid interface, located in the bulk of the domain $x \in [0, l]$, physically meaningful boundary conditions are

$$\psi(0) = -1, \psi(l) = 1 \quad (13)$$

provided that the width of the interface is much smaller than the distances between this interface and the boundaries $x = 0$ and $x = l$. As one can judge from the $\Phi(x) = \frac{1}{2}(1 + \psi(x))$ plots in [20], the boundary conditions (13) are always used in that paper, even if the phase boundary is just at the surface $x = 0$.

We propose an original method, allowing that $\psi(x)$ is quite different from -1 at $x = 0$ or quite different from 1 at $x = l$. We will further introduce boundary conditions of a new type, allowing to describe such cases. Our new approach is useful for a description of situations, where the phase boundary is close to a border of the domain $x \in [0, l]$, including also the final steps of the solidification process.

One of our basic assumptions is that the shape of the solid-liquid interface at the beginning of the melting process is similar to its equilibrium shape. The latter one is consistent with the equation $\partial \psi / \partial t = 0$ at $u = 0$, or

$$\epsilon^2 \frac{\partial^2 \psi}{\partial x^2} + \psi - \psi^3 = 0 \quad (14)$$

The solution of (14), which satisfies the conditions $\psi(-\infty) = -1$ and $\psi(\infty) = 1$, is

$$\psi(x) = \tanh\left(\frac{x - x_0}{\sqrt{2}\epsilon}\right) \quad (15)$$

with an arbitrary parameter x_0 . Our assumption is self consistent within the simulations we performed, as we observed that the shape of the interface is always very similar to (15), even for the moving interface at $u \neq 0$. Obviously, there is no need to assume $\psi(0) = -1$ as the boundary condition, since there exists the equilibrium shape with any value of $\psi(0)$ within $]-1, 1[$ corresponding to $x_0 = -\frac{\epsilon}{\sqrt{2}} \ln\left(\frac{1 + \psi(0)}{1 - \psi(0)}\right)$ in (15). It is also physically meaningful to set a larger than -1 value of $\psi(0)$ at the very beginning of the melting process, to describe the situation, where the near-to-surface layer is not yet completely melted.

We propose an approximation, where the phase field is introduced discontinuously by setting $\psi(x) = B \tanh\left(\frac{x - x_0}{\sqrt{2}\epsilon}\right)$ at the time moment $t = t_1$, when the melting temperature is reached (u becomes positive) at a small distance from the surface, i.e., at $x = x_0 = A\sqrt{2}\epsilon$, where A is a

positive constant. We have set $A = 0.5$ as a standard, in which case the plot of $\psi(x)$ is moderately cut by the surface boundary at the beginning. The distance x_0 is small as compared to l due to the smallness of $\epsilon \ll l$.

The constant B is set $B = 1/\tanh\left(\frac{l-x_0}{\sqrt{2}\epsilon}\right) \approx 1$ to ensure that $\psi(l) = 1$ holds.

Practically, B is almost precisely 1 in our simulations, since $l-x_0 \gg \sqrt{2}\epsilon$. Consequently, the initial $\psi(x)$ shape is almost the equilibrium one (15), in accordance with our basic assumption.

The boundary conditions for $\psi(x)$ are chosen consistently: for the interface centered at the coordinate x_0 , where x_0 is generally defined by $\psi(x_0) = 0$, we set

$$\begin{cases} \psi(l) = 1, \psi(0) = -\psi(2x_0) \text{ if } x_0 < l/2, \\ \psi(0) = -1, \psi(l) = -\psi(2x_0 - l) \text{ if } x_0 > l/2. \end{cases} \quad (16)$$

The initial $\psi(x)$ function at $t = t_1$ satisfies these conditions, and we require them at $t \geq t_1$. The values of x_0 and $\psi(2x_0)$ (if $x_0 < l/2$) or $\psi(2x_0 - l)$ (if $x_0 > l/2$) at $t > t_1$ are determined by a linear interpolation of $\psi(x)$. The advantage of (16) in comparison with (13) is that the shape of $\psi(x)$ is practically not distorted when x_0 comes close to 0 or l , i.e., it is always quite similar to the equilibrium shape. The $\psi(x)$ plot is only cut off from that side, which is close to the boundary. Both variants (13) and (16) are equivalent when the distances from the boundaries, i.e., x_0 and $l - x_0$, are much larger than the characteristic half-width of the interface, which is about $\sqrt{2}\epsilon$.

The $\psi(x)$ profile moves into the depth during the melting process, and then it moves back during the solidification process after the laser pulse. We have assumed that the solidification process is finished at $t = t_2$ when x_0 reaches the point $x_0 = A\sqrt{2}\epsilon$. Thus, the final $\psi(x)$ profile is similar to the initial one. We have aware that the resulting final $c(x)$ segregation profile is insignificantly influenced by the choice of A value within $0.1 \leq A \leq 0.5$.

A modeling problem is that the GeSn layer can be completely melted during some time interval. Formally, it corresponds to $\psi(x) \equiv -1$. One can try to model a transition to this state and afterwards the inverse transition. However, we have found a simpler formal solution of this problem. Namely, we formally solve (10)-(11) within the whole time domain $t \in [t_1, t_2]$, and only “switch off” the phase field in (9) by setting $\nabla\psi = 0$ at the melting condition $x_0 > l - A\sqrt{2}\epsilon$. Eqs. (10)-(11) with our boundary conditions do not describe the complete melting and, formally, a small amount of GeSn material remains solid in the vicinity of the boundary $x = l$. (According to our numerical procedures, x_0 approaches, but not reaches l .) However, it is not harmful for the heat balance in (7) and also for the impurity redistribution under the application of our “switching off” procedure.

The proposed here original treatment concerning the initialization of the solid-liquid interface and the usage of the boundary conditions (16) is essential for reproducing the monotonously decaying shape of the $c(x)$ profile near the surface, observed in our experiments. If the boundary conditions (13) are used instead of (16), then the motion of $\psi(x)$ profile tends to stop at some distance (with x_0 about $\sqrt{2}\epsilon$) from the surface in the solidification process. It results into the $c(x)$ profile with maximum at $x > 0$, if the process is terminated at $x_0 = \sqrt{2}\epsilon$ due to the fact that no essentially smaller values of x_0 can be reached. Hence, (16) allows to describe the solid-liquid interface closer to the surface (e.g., at $x_0 = 0.1\sqrt{2}\epsilon$, corresponding to $A = 0.1$) as compared to (13).

The actual calculation algorithm has been implemented in the FORTRAN code. This code with description (as a commented text inside the code file) is attached as the Supplement.

2.3. Stability and accuracy tests

We have performed a numerical stability analysis of our finite difference scheme using test calculations at various spatial grid step sizes Δx and time steps Δt . These calculations have been performed at certain optimal parameters of the model further discussed in detail in Section 3.

The dimensionless grid step size $\tilde{\Delta x} = \Delta x/L_{\text{diff}}$ and the dimensionless time step $\tilde{\Delta t} = \Delta t/t_{\text{pulse}}$ were considered, where $L_{\text{diff}} = 465\text{nm}$ is (approximately) the heat diffusion length in pure Ge during the laser pulse. Based on test calculations for $\Delta x = 0.01, 0.005, 0.0025$ and 0.00125 at various $\tilde{\Delta t}$, we have found that our difference scheme obeys the known stability criterion [30] for explicit difference schemes applied to drift-diffusion equations, according to which the solution is numerically stable at the condition $0 < \tilde{\Delta t}/(\tilde{\Delta x})^2 < C$, where C is some constant. We have evaluated $C \approx 0.625$ in our case. Hence, the stability border for $\tilde{\Delta x} = 0.0025$ is located at $\tilde{\Delta t} \approx 3.906 \cdot 10^{-6}$. We have used the values $\tilde{\Delta t} = 2.5 \cdot 10^{-6}$ and $\tilde{\Delta x} = 0.0025$ as a standard in most of our simulations. To test the influence of $\tilde{\Delta t}$, some calculations were performed at $\tilde{\Delta t} = 1.25 \cdot 10^{-6}$ for $\tilde{\Delta x} = 0.0025$. The $\psi(x)$ and $c(x)$ profiles near the solid-liquid interface in the middle of the solidification process (at $\tilde{\tau} = t/t_{\text{pulse}} = 13$) after the first laser pulse are compared in Fig. 2. The results for $\tilde{\Delta t} = 2.5 \cdot 10^{-6}$ are shown by solid lines, whereas those for $\tilde{\Delta t} = 1.25 \cdot 10^{-6}$ – by circles. In fact, the corresponding curves lie on top of each other. We have checked this also for later times moments, i. e., at the end of the solidification process after the first pulse and after the tenth pulse, as shown in Fig. 3. As before, the corresponding curves lie on top of each other. It provides a strong evidence that the method is numerically stable at $\tilde{\Delta t} = 2.5 \cdot 10^{-6}$ and $\tilde{\Delta x} = 0.0025$, and the error of integration over time is negligibly small in this case. The reason for small integration error, obviously, is the very small $\tilde{\Delta t}$ value chosen due to the stability constraint. A faster integration with a significantly larger time step would be, eventually, possible by using an implicit difference scheme, e.g., the Crank-Nicolson scheme [31].

We have also tested the influence of the spatial step size $\tilde{\Delta x}$. For this purpose, test calculations were performed at $\tilde{\Delta x} = 0.00125$ and $\tilde{\Delta t} = 0.625 \cdot 10^{-6}$, the latter value being chosen 4 times smaller than that for $\tilde{\Delta x} = 0.0025$ due to the stability constraint. The results are shown by dashed lines in Figs. 2 and 3. Comparing with the corresponding (solid) curves at $\tilde{\Delta x} = 0.0025$ and $\tilde{\Delta t} = 2.5 \cdot 10^{-6}$, we can see some systematic shifts. These shifts are quite insignificant in Fig. 2, resulting in a small time delay in the motion of $\psi(x)$ and $c(x)$ profiles. There is a very small difference seen in Fig. 3, except only the vicinity of the surface, where the refined calculation with $\tilde{\Delta x} = 0.00125$ gives a slightly larger Sn

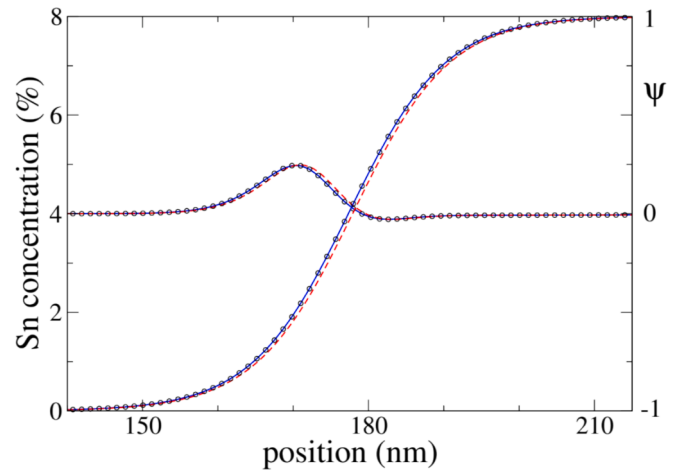


Fig. 2. The $c(x)$ (non-monotonous curves, left axis) and $\psi(x)$ (monotonous curves, right axis) profiles in the region of the solid-liquid interface at the time moment $t/t_{\text{pulse}} = 13$ during the solidification process after the first laser pulse. The results for different step sizes, i.e., $\tilde{\Delta x} = 0.0025, \tilde{\Delta t} = 2.5 \cdot 10^{-6}$ (solid curves), $\tilde{\Delta x} = 0.0025, \tilde{\Delta t} = 1.25 \cdot 10^{-6}$ (circles) and $\tilde{\Delta x} = 0.00125, \tilde{\Delta t} = 0.625 \cdot 10^{-6}$ (dashed curves) are shown.

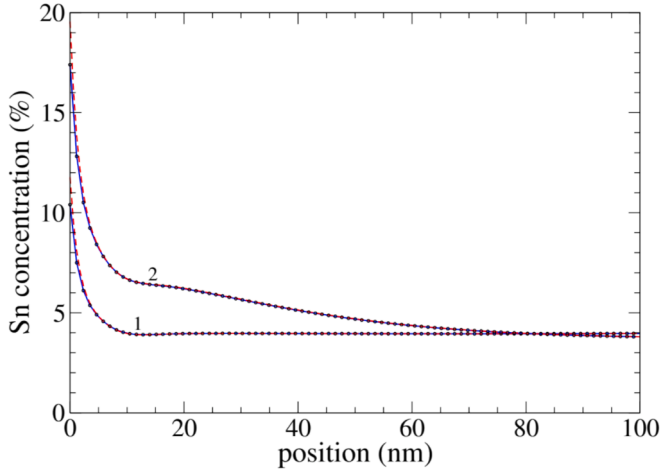


Fig. 3. The $c(x)$ profiles near the surface at the end of the solidification process after the first (1) and after the tenth (2) laser pulse. The results for different step sizes, i.e., $\Delta x = 0.0025$, $\Delta t = 2.5 \cdot 10^{-6}$ (solid curves), $\Delta x = 0.0025$, $\Delta t = 1.25 \cdot 10^{-6}$ (circles) and $\Delta x = 0.00125$, $\Delta t = 0.625 \cdot 10^{-6}$ (dashed curves) are shown.

concentration at the surface and within a 1nm layer near the surface. This difference is not relevant for an approximate comparison with experimental data discussed further on.

3. Simulation of the GeSn/Si structure

We have performed the simulation of the Sn redistribution in the GeSn/Si structure, using the method described in Sec. 2. Considering dimensionless quantities, we have normalized the time to $t_{\text{pulse}} = 6\text{ns}$ and all distances to the heat diffusion length $L_{\text{diff}} = \sqrt{D_{\text{heat}} t_{\text{pulse}}} \approx 465\text{nm}$ in pure Ge, where $D_{\text{heat}} \approx 0.36\text{cm}^2/\text{s}$ [32]. The relaxation time of the local interface arrangement of atoms is expected to be on the picosecond rather than nanosecond range, therefore we have set $\tilde{\tau} = 0.01$ for the dimensionless relaxation time, corresponding to the limit $\tilde{\tau} \ll 1$. The precise value of $\tilde{\tau}$ is not important in this case. The width of the interface, which is $\approx 2\sqrt{2}\epsilon$ in our model (see Sec. 2.2), could be of the order of few nanometers, assuming that the interface consists of several atomic layers. Thus, the dimensionless parameter $\tilde{\epsilon} = \epsilon/L_{\text{diff}}$ can be even smaller than 0.01. However, it is technically difficult to perform calculations with a very narrow interface, therefore we have set $\tilde{\epsilon} = 0.02$, corresponding to $\approx 26\text{nm}$ width of the interface. The results are slightly influenced by the value of $\tilde{\epsilon}$. The third parameter λ in (10) has to be set $\lambda \gg 1$ to ensure that the temperature at the interface is reasonably close to T_m . The precise value is not important in this limit, and we have used $\lambda = 10$.

Some of the thermal parameters have been assumed to be approximately the same for GeSn and pure Ge. Indeed, the considered here average or effective parameters correspond to the mean Sn concentration (c) ≈ 0.04 , which is quite small. However, we take into account that the heat conductivity and diffusivity can be essentially affected by the scattering of phonons on impurities even for a small impurity concentration. Thus, we have used the melting temperature $T_m^{\text{GeSn}} \approx T_m^{\text{Ge}} \approx 1211\text{K}$, the heat of fusion $L^{\text{GeSn}} \approx L^{\text{Ge}} \approx 508.6\text{J/g}$, as well as specific heat values $c_p^{\text{GeSn}} \approx c_p^{\text{Ge}} \approx 0.35\text{J g}^{-1}\text{K}^{-1}$ and $c_p^{\text{Si}} \approx 0.9\text{J g}^{-1}\text{K}^{-1}$ for GeSn and Si at high temperatures [32]. It corresponds to the dimensionless parameter $b = 0.828$ in (9) and the initial u value $u_0 = -0.6215$. The heat diffusivity of Si varies significantly with temperature [33]. We have assumed $D_{\text{heat}}^{\text{Si}} \approx 0.3\text{cm}^2/\text{s}$, or $\tilde{D}_{\text{heat}}^{\text{Si}} = 0.8$ in the dimensionless form as an average value for the temperature interval from 300 K to about 1200 K reached in Si.

The heat conductivity of pure Ge decreases from $\approx 60\text{Wm}^{-1}\text{K}^{-1}$ at room temperature to a value about $17.3\text{Wm}^{-1}\text{K}^{-1}$ at $T = 1200\text{K}$ [34]. It is about $14.3\text{Wm}^{-1}\text{K}^{-1}$ for GeSn with $c \approx 0.033$ (the mean value within $x \in [0, l]$, where $l = 385\text{nm}$) at room temperature, obtained as the average value of two measurement methods discussed in [7]. We have used a simple theoretical model to evaluate the heat diffusivity $D_{\text{heat}}^{\text{GeSn}}$ of GeSn near $T_m \approx 1211\text{K}$ from these data. Note that Ge and GeSn are semiconductors, and we observe a decrease of heat conductivity with increasing temperature. Hence, we assume that the heat is conducted mainly by the lattice. The heat conductivity is considered as being proportional to the phonon lifetime τ_{ph} . Applying a similar model as in [35], we have

$$\frac{1}{\tau_{\text{ph}}} = \frac{1}{\tau_{\text{ph-ph}}} + \frac{1}{\tau_{\text{ph-imp}}} \quad (17)$$

where $\tau_{\text{ph-ph}}$ and $\tau_{\text{ph-imp}}$ are the lifetimes corresponding to the phonon-phonon and phonon-impurity scattering mechanisms, respectively. The first one basically depends on the impurity concentration c , whereas the second one depends on the lattice temperature. We find from the data of [7] that $1/\tau_{\text{ph-imp}}$ exceeds $1/\tau_{\text{ph-ph}}$ by the factor of ≈ 3.2 at room temperature. On the other hand, $1/\tau_{\text{ph-ph}}$ increases by the factor of ≈ 3.5 when the temperature rises to 1200 K according to the data of [34]. Thus, $1/\tau_{\text{ph-imp}} \approx 0.9/\tau_{\text{ph-ph}}$ holds at high temperatures near T_m . Hence, the heat conductivity κ of GeSn is evaluated to be roughly 1.9 times smaller than that of pure Ge near T_m . The same is true for the heat diffusivity $D_{\text{heat}} = \frac{\kappa}{\rho c_p}$, where ρ is the density.

Thus, using the data $D_{\text{heat}}^{\text{Ge}} \approx 0.093\text{cm}^2/\text{s}$ of pure Ge near T_m [34], we obtain $D_{\text{heat}}^{\text{GeSn}} \approx 0.049\text{cm}^2/\text{s}$ or $\tilde{D}_{\text{heat}}^{\text{GeSn}} \approx 0.136$ for GeSn with $c \approx 0.033$ at $T \approx T_m$. These values refer to the solid phase. For comparison, the heat diffusivity of liquid Ge near T_m is about $0.18\text{cm}^2/\text{s}$ according to the data in [36,37]. We note that just $\tilde{D}_{\text{heat}}^{\text{GeSn}}$ of solid phase at $T \approx T_m$ is a relevant parameter, as it governs the heat flux from the melted GeSn region through the solid GeSn region into the bulk and, consequently, the velocity of motion of the solid-liquid interface during the solidification process. Therefore, we have used $\tilde{D}_{\text{heat}}^{\text{GeSn}} = 0.136$ as one of the effective parameters in our simulations. One more parameter, used in the calculation of the heat flux, is the ratio $\kappa_{\text{Si}}/\kappa_{\text{GeSn}}$, which appears in the boundary condition at the GeSn/Si interface. It has been evaluated as $\kappa_{\text{Si}}/\kappa_{\text{GeSn}} = 1.125 \left(\frac{\tilde{D}_{\text{heat}}^{\text{Si}}}{\tilde{D}_{\text{heat}}^{\text{GeSn}}} \right)$, using the c_p and ρ data of Si and GeSn.

Considering the parameters of the heat source, we have set $\alpha L_{\text{diff}} = 0.395$ for the dimensionless absorption coefficient in accordance with $\alpha = 8.5 \cdot 10^3 \text{cm}^{-1}$ for strained GeSn [38]. The dimensionless intensity of the source was chosen $g_0 t_{\text{pulse}} = 4.2$, slightly exceeding the threshold value at which the GeSn layer is completely melted.

We need the value of the Sn diffusion coefficient D_L in the liquid phase of GeSn contained in the flux equation (9). It is about $2 \cdot 10^{-5}\text{cm}^2/\text{s}$ near T_m according to the data of [36], corresponding to the dimensionless diffusion coefficient $\tilde{D}_L = 0.000056$ used in our calculations.

A relevant parameter in (9) is $\Delta\epsilon$. It is related to the equilibrium segregation coefficient

$$k_s = \exp\left(-\frac{E_S - E_L}{k_B T_m}\right) = \exp\left(-\frac{\Delta\epsilon}{b}\right) \quad (18)$$

The value of k_s for Sn in Ge is about 0.017 [39], therefore we have set $\Delta\epsilon = 3.14$ according to (18). The parameter v in (9) affects the energy landscape $\Delta E(\psi) = E(\psi) - E_L$ and the interfacial barrier of the potential energy when an Sn atom moves from solid to liquid phase. We have considered it as an adjustable parameter, evaluated by comparing the simulation results with the experimental concentration profile after 98 laser pulses, in accordance with the laser processing described in [27].

The initial Sn distribution in our simulations, as well as the thickness and parameters of the GeSn layer correspond approximately to this experiment. The comparison for $\nu/\Delta\varepsilon = 0, 0.5, 1, 1.5$ and the corresponding energy landscapes are shown in Fig. 4. The calculated concentration distribution is not quite well consistent with the experimental profile at $\nu = 0$, i.e., in absence of any potential barrier. The choice $\nu = \Delta\varepsilon$ (thick solid curves) with some potential barrier (about 0.2 eV) appears to be nearly optimal.

The dynamics of the observed Sn segregation process in the GeSn/Si structure at $\nu = \Delta\varepsilon$ is illustrated in Fig. 5, where the initial Sn distribution, as well as the intermediate concentration profiles after 1, 10 and 30 laser pulses are also shown.

The calculation results show a certain accumulation of Sn concentration near the surface when the melting and solidification process is repeated. The final $c(x)$ profile (thick solid curve) is in a qualitative agreement with the experimental profile obtained by the energy dispersive spectroscopy (thick dashed curve) [27]. X-ray photoelectron spectroscopy verified 28 % Sn concentration on the very surface [11]. For a better quantitative agreement, a refining of the theoretical model could be helpful. The observed effect of increasing $c(x)$ near the surface results from the segregation of Sn atoms by the moving solid–liquid interface. It is illustrated in Fig. 6 for the first pulse. A similar picture repeats from pulse to pulse, however, with some accumulation and saturation effect. In each pulse, a fraction of Sn atoms is moved as a package toward the surface, in such a way that the $c(x)$ distribution at the end of the solidification process after each pulse is a smooth function with maximum at $x = 0$.

4. Discussion

The calculated Sn concentration profile after 98 laser pulses (Fig. 5, Sec. 3) is in a qualitative agreement with the experimental data at a reasonable choice of the parameters in the model. In particular, a significant increase of the Sn concentration near the surface is observed due to the segregation effect accumulated over many laser pulses. However, the quantitative agreement is not perfect, and there is a room for improvements. In particular, the resulting concentration profile could be modified by the interaction between Sn atoms, which is not yet included in the model. It could be also affected by nonhomogeneous variations in the thermal and optical properties of the GeSn material, as a feedback from the redistribution of Sn atoms.

Our model has been applied to the GeSn material, however, it can be useful for predicting the concentration (segregation) profiles in any two-component system. There is practically no restrictions to the initial concentration profile, except that the concentration should be not too large. Namely, the results are expected to be better for smaller impurity

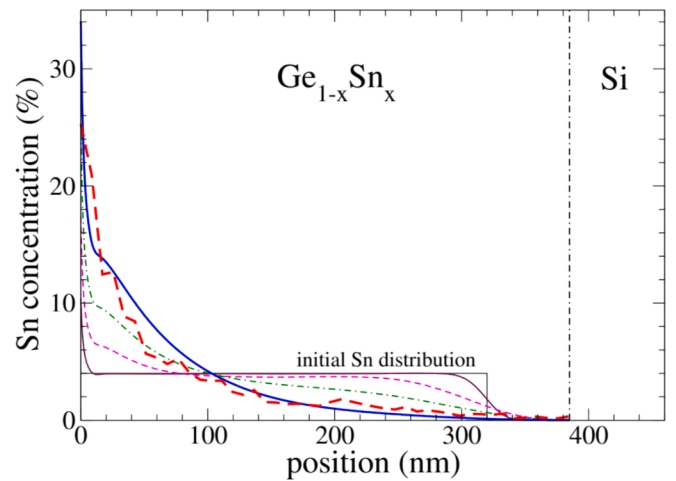


Fig. 5. The calculated (thick solid curve) and experimental (thick dashed curve) Sn concentration profiles in $\text{Ge}_{1-x}\text{Sn}_x/\text{Si}$ structure after 98 laser pulses. The calculated intermediate profiles after one pulse (thin solid curve) and 10 pulses (dashed curve) and 30 pulses (dot-dashed curve) are also shown. The initial Sn profile is represented by the rectangle. It corresponds to the experimental data in [27].

concentration, as we have neglected the interaction between impurities and the feedback from their redistribution. There is also a restriction that the thickness of the layer, containing the solid–liquid interface, should be significantly larger than the width of this interface to justify the usage of the boundary conditions (16).

The developed here model allowed us to describe the increase of Sn content in GeSn solid solution up to 28 % observed in our laser experiments [11]. An essential question is about the peculiarities of the physical mechanism allowing to reach so high Sn concentration, which is not achievable by other known methods, according to our knowledge. In particular, 15 to 18 percents have been reached in GeSn epitaxial layers grown by molecular beam epitaxy method [40]. However, the obtained GeSn layers become non-homogeneous with metallic Sn inclusions in this case. It results in defects, like dislocations, and enhanced surface roughness [40]. As a result, the quality of the obtained GeSn layer appears to be unsatisfactory for applications in electronic devices. To the contrary, the layers obtained by the laser irradiation still have a high quality without metallic inclusions even at 28 % of Sn concentration.

A fundamental question is why the Sn inclusions are formed by the molecular beam method, but not by the laser method. We explain it

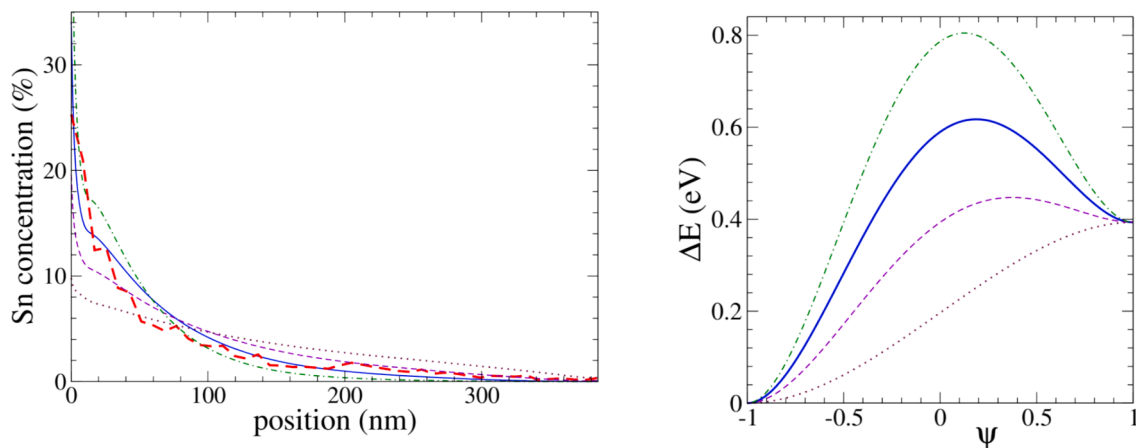


Fig. 4. The calculated $c(x)$ distributions after 98 laser pulses (left) and the corresponding energy landscapes (right) at $\nu/\Delta\varepsilon = 0$ (dotted curves), $\nu/\Delta\varepsilon = 0.5$ (thin dashed curves), $\nu/\Delta\varepsilon = 1$ (solid curves) and $\nu/\Delta\varepsilon = 1.5$ (dot-dashed curves). The experimental Sn concentration profile is shown by the thick dashed line.

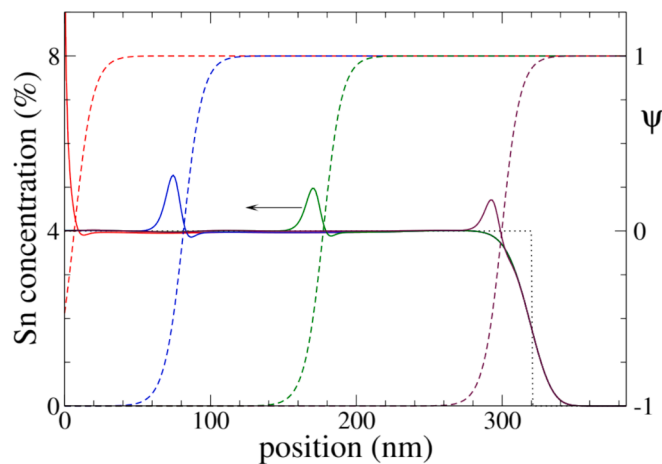


Fig. 6. The concentration $c(x)$ (solid curves, left axis) and the phase field $\psi(x)$ (dashed curves, right axis) profiles at the time moments $\tilde{t} = t/t_{\text{pulse}} = 8, 13, 18, 22.6$ with \tilde{t} increasing in the direction of motion, indicated by the arrow. The latter time moment corresponds approximately to the end of the solidification process after the first laser pulse considered here. The initial concentration profile is shown by the dotted line.

basically by the fact that the solidification and recrystallization process after a laser pulse takes place on a much shorter time scale than the formation of GeSn material from the deposited Ge and Sn atoms in the molecular beam epitaxy process. As one can judge from Fig. 6, the solid–liquid phase boundary moves with a speed about 3 nm/ns in the solidification process after a laser pulse. For comparison, the speed of the epitaxial growth in the molecular beam deposition process is 0.1 nm/s, as reported in [40]. Thus, the process appears to be $3 \cdot 10^{10}$ times faster after a laser pulse. One should recall that a homogeneous GeSn solid solution with a high Sn content is metastable, since the equilibrium solubility of Sn in Ge is $<1\%$ [27]. As a consequence, Sn tends to form metallic inclusions (a separate phase) at higher Sn concentrations in equilibrium. However, their formation requires some equilibration time, which can be very long at room temperature. It reveals a possibility to form GeSn solid solution with a high Sn content (which is metastable, but practically stable at room temperature), if the process is fast enough and the formed metastable solid solution is quenched due to a rapid cooling at the end of the process. This, as we believe, is just what happens in our laser processing.

The question why a similar result is not obtained by the molecular beam epitaxy is not quite trivial, because the sputtering is carried out at a relatively low temperature, i.e., at 160 °C or 140 °C [40]. For comparison, the melting temperature of GeSn is reached in the laser processing. It is totally expected that the equilibration process, resulting into the formation of Sn inclusions, proceeds slower at a lower temperature. Hence, there are two competing factors, i.e., the time scale and the temperature, which have to be taken into account. The combination of both these factors are in favor of the formation of GeSn solid solution without the metallic Sn inclusions in the laser processing, and the formation of such inclusions in the molecular beam epitaxy process. This can be concluded from the experimental results [27,40]. From the modeling point of view, this is still a future challenge to develop such a model, which would be able to describe both cases. The actual model does not include any mechanisms of phase separation, potentially resulting into formation of separate Sn inclusions. This would be a 3D problem, since these inclusions are 3D objects. The actual 1D model is valid for the melting and solidification process if such 3D objects do not emerge, as in our laser experiments.

5. Conclusions

In this paper, a phase field model has been used to describe the

impurity redistribution in a rapid solidification process. In fact, we have extended (in Sec. 2.1) the known phase field model of solidification in pure melt [15–18], including the heat source and impurities into the consideration, as well as modeling the emergence of the solid–liquid interface by an original method, applying new boundary conditions (Section 2.2). This extension is distinct from the one proposed earlier in [19–22]. In particular, the equations, derived here, are suited not only for treating the two-phase system, but can also be used for a single phase, where the impurity redistribution is driven by the temperature gradient. These equations have been implemented for the description of a complex process in GeSn/Si structure, consisting of the laser heating of solid phase, melting and solidification process (Sec. 2.2). We have used a simple explicit difference scheme for solving these equations, providing a strong numerical evidence of its stability at small enough time steps (Sec. 2.3). Calculations for the GeSn/Si structure have been performed (Sec. 3), showing a qualitative agreement with the experimental data.

CRediT authorship contribution statement

Jevgenijs Kaupužs: Writing – review & editing, Writing – original draft, Supervision, Software, Methodology, Investigation, Formal analysis, Data curation, Conceptualization. **Pavels Onufrijevs:** Writing – review & editing, Writing – original draft, Project administration, Funding acquisition, Formal analysis, Data curation, Conceptualization. **Patrik Šcajev:** Writing – review & editing, Writing – original draft, Investigation, Data curation, Conceptualization. **Hung Hsiang Cheng:** Writing – original draft, Supervision, Project administration, Investigation, Formal analysis, Data curation, Conceptualization. **Guo-En Chang:** Writing – review & editing, Writing – original draft, Methodology, Investigation, Data curation, Conceptualization. **Yoshishige Tsuchiya:** Writing – review & editing, Writing – original draft, Supervision, Project administration, Investigation, Conceptualization.

Declaration of competing interest

The authors declare that they have no known competing financial interests or personal relationships that could have appeared to influence the work reported in this paper.

Acknowledgements

The authors gratefully acknowledge the ERA-NET Cofund project CHIST-ERA supported by the Horizon Europe: “NOEMIA - Nano-Opto-Electro-Mechanical Integrated Oscillator Arrays for Energy-Efficient Physical Reservoir Computing” Nr. ES RTD/2023/16 and NSTC 112-2923-M-002 -004 -MY3. P.O. and P.Š. acknowledge the European Cooperation in Science and Technology (COST) action: “European Network for Innovative and Advanced Epitaxy” (CA20116, P-COST-21-6, 2021–2025). The authors acknowledge the Latvian Grid Infrastructure and High-Performance Computing Centre of Riga Technical University for providing resources.

Appendix A. Supplementary data

Supplementary data to this article can be found online at <https://doi.org/10.1016/j.optlastec.2025.113046>.

Data availability

Data will be made available on request.

References

- [1] C.-H. Liu, R. Bansal, C.-W. Wu, Y.-T. Jheng, G.-E. Chang, GeSn Waveguide Photodetectors with Vertical p–i–n Heterostructure for Integrated Photonics in the 2 μm wavelength band, *Adv. Photonics Res.* 3 (2022) 1–8, <https://doi.org/10.1002/adpr.202100330>.

- [2] H. Tran, T. Pham, J. Margetis, Y. Zhou, W. Dou, P.C. Grant, et al., Si-based GeSn photodetectors toward mid-infrared imaging applications, *ACS Photonics* 6 (2019) 2807–2815, <https://doi.org/10.1021/acsp Photonics.9b00845>.
- [3] K.C. Lee, M.X. Lin, H. Li, H.H. Cheng, G. Sun, R. Soref, et al., Planar GeSn photodiode for high-detectivity photodetection at 1550 nm, *Appl. Phys. Lett.* 117 (2020), <https://doi.org/10.1063/5.0006711>.
- [4] K.P. Homewood, M.A. Lourenço, The rise of the GeSn laser, *Nat. Photonics* (2015), <https://doi.org/10.1038/nphoton.2015.1>.
- [5] B. Marzban, L. Seidel, T. Liu, K. Wu, V. Kiyek, M.H. Zoellner, et al., Strain engineered electrically pumped SiGeSn microring lasers on Si, *ACS Photonics* 10 (2023) 217–224, <https://doi.org/10.1021/acsp Photonics.2c01508>.
- [6] Y. Junk, O. Concepción, M. Frauenrath, J. Sun, J.H. Bae, F. Bärfwolf, et al., Enhancing Device Performance with High Electron Mobility GeSn Materials, *Adv. Electron. Mater.* (2024), <https://doi.org/10.1002/aem.202400561>.
- [7] O. Concepción, J. Tiscareño-Ramírez, A.A. Chimienti, T. Classen, A.A. Corley-Wiciak, A. Tomadin, et al., Room temperature lattice thermal conductivity of GeSn alloys, *ACS Appl. Energy Mater.* 7 (2024) 4394–4401, <https://doi.org/10.1021/acsaem.4c00275>.
- [8] M.P. Polak, P. Scharoch, R. Kudrawiec, The electronic band structure of Ge 1–x Sn x in the full composition range: indirect, direct, and inverted gaps regimes, band offsets, and the Burstein-Moss effect, *J. Phys. D Appl. Phys.* 50 (2017) 195103, <https://doi.org/10.1088/1361-6463/aa67bf>.
- [9] S.A. Ghetmiri, W. Du, J. Margetis, A. Mosleh, L. Cousar, B.R. Conley, et al., Direct-bandgap GeSn grown on silicon with 2230 nm photoluminescence, *Appl. Phys. Lett.* 105 (2014), <https://doi.org/10.1063/1.4898597>.
- [10] W. Dou, M. Benamara, A. Mosleh, J. Margetis, P. Grant, Y. Zhou, et al., Investigation of GeSn strain relaxation and spontaneous composition gradient for low-defect and high-Sn alloy growth, *Sci. Rep.* 8 (2018) 5640, <https://doi.org/10.1038/s41598-018-24018-6>.
- [11] P. Ščajev, P. Onufrijevs, A. Mekys, T. Malinauskas, D. Augulis, L. Subačius, et al., Extension of Spectral Sensitivity of GeSn IR Photodiode after Laser Annealing, *Appl. Surf. Sci.* 555 (2021) 149711, <https://doi.org/10.1016/j.apsusc.2021.149711>.
- [12] M. Frauenrath, P. Acosta Alba, O. Concepción, J.-H. Bae, N. Gauthier, E. Nolot, et al., Nanosecond laser annealing of pseudomorphic GeSn layers: Impact of Sn content, *Mater. Sci. Semicond. Process.* 163 (2023) 107549, <https://doi.org/10.1016/j.mssp.2023.107549>.
- [13] M.T. Islam, M.C. Gupta, Polycrystalline GeSn thin films fabricated by simultaneous laser sintering and recrystallization, *J. Mater. Sci. Mater. Electron.* 34 (2023) 272, <https://doi.org/10.1007/s10854-022-09703-7>.
- [14] E. Talamas Simola, V. Kiyek, A. Ballabio, V. Schlykow, J. Frigerio, C. Zucchetti, et al., CMOS-compatible bias-tunable dual-band detector based on GeSn/Ge/Si coupled photodiodes, *ACS Photon.* 8 (2021) 2166–2173, <https://doi.org/10.1021/acsp Photonics.1c00617>.
- [15] J.S. Langer, *Directions In Condensed Matter Physics: Memorial Volume In Honor Of Shang-keng Ma*, World Scientific Publishing Company, 1986.
- [16] D.A. Kessler, J. Koplik, H. Levine, Pattern selection in fingered growth phenomena, *Adv. Phys.* 37 (1988) 255–339, <https://doi.org/10.1080/00018738800101379>.
- [17] A. Karma, W.J. Rappel, Phase-field method for computationally efficient modeling of solidification with arbitrary interface kinetics, *Phys. Rev. E – Stat. Phys. Plasmas Fluids Relat. Interdiscip. Top* 53 (1996) R3017–R3020, <https://doi.org/10.1103/PhysRevE.53.R3017>.
- [18] A. Karma, W.-J. Rappel, Quantitative phase-field modeling of dendritic growth in two and three dimensions, *PhysRevE* 57 (1998) 4323–4349, <https://doi.org/10.1103/PhysRevE.57.4323>.
- [19] N.A. Ahmad, A.A. Wheeler, W.J. Boettinger, G.B. McFadden, Solute trapping and solute drag in a phase-field model of rapid solidification, *PhysRevE* 58 (1998) 3436–3450, <https://doi.org/10.1103/PhysRevE.58.3436>.
- [20] A. La Magna, P. Alippi, V. Privitera, G. Fortunato, M. Camalleri, B. Svensson, A phase-field approach to the simulation of the excimer laser annealing process in Si, *J. Appl. Phys.* 95 (2004) 4806–4814, <https://doi.org/10.1063/1.1690861>.
- [21] A. La Magna, P. Alippi, V. Privitera, G. Fortunato, Role of light scattering in excimer laser annealing of Si, *Appl. Phys. Lett.* 86 (2005), <https://doi.org/10.1063/1.1906318>.
- [22] R. Milazzo, E. Napolitani, G. Impellizzeri, V. Privitera, A. La Magna, Laser annealing in Si and Ge: Anomalous physical aspects and modeling approaches, *Mater. Sci. Semicond. Process.* 62 (2017) 80–91, <https://doi.org/10.1016/j.mssp.2016.10.047>.
- [23] D. Mokbel, H. Abels, S. Aland, A phase-field model for fluid–structure interaction, *J. Comput. Phys.* 372 (2018) 823–840, <https://doi.org/10.1016/j.jcp.2018.06.063>.
- [24] N. Valizadeh, X. Zhuang, T. Rabczuk, A monolithic finite element method for phase-field modeling of fully Eulerian fluid–structure interaction, *Comput. Methods Appl. Mech. Eng.* 435 (2025) 117618, <https://doi.org/10.1016/j.cma.2024.117618>.
- [25] Z. Wen, N. Valizadeh, T. Rabczuk, X. Zhuang, Hydrodynamics of multicomponent vesicles: A phase-field approach, *Comput. Methods Appl. Mech. Eng.* 432 (2024) 117390, <https://doi.org/10.1016/j.cma.2024.117390>.
- [26] E. Samaniego, C. Anitescu, S. Goswami, V.M. Nguyen-Thanh, H. Guo, K. Hamdia, et al., An energy approach to the solution of partial differential equations in computational mechanics via machine learning: Concepts, implementation and applications, *Comput. Methods Appl. Mech. Eng.* 362 (2020) 112790, <https://doi.org/10.1016/j.cma.2019.112790>.
- [27] P. Onufrijevs, P. Ščajev, A. Medvids, M. Andrulevicius, S. Nargelas, T. Malinauskas, et al., Direct-indirect GeSn band structure formation by laser Radiation: The enhancement of Sn solubility in Ge, *Opt. Laser Technol.* 128 (2020) 106200, <https://doi.org/10.1016/j.optlastec.2020.106200>.
- [28] V.P. Voronkov, G.A. Gurchenok, Impurity diffusion in semiconductors at laser annealing of semiconductors, *Phys. Technol. Semicond.* 24 (1990) 1831–1834.
- [29] D. Zhao, A. Würger, X. Crispin, Ionic thermoelectric materials and devices, *J Energy Chem* 61 (2021) 88–103, <https://doi.org/10.1016/j.jechem.2021.02.022>.
- [30] J.W. Thomas, *Numerical Partial Differential Equations: Finite Difference Methods*, vol. 22, Springer New York, New York, NY, 1995. doi: 10.1007/978-1-4899-7278-1.
- [31] T. Cebeci, *Convective Heat Transfer*, Springer, Berlin Heidelberg, 2002.
- [32] A.S. Okhotin, A.S. Pushkarskij, V.V. Gorbachev, *Thermophysical Properties of Semiconductors*, Atomizdat, USSR, 1972.
- [33] H.R. Shanks, P.D. Maycock, P.H. Siddles, G.C. Danielson, Thermal Conductivity of Silicon from 300 to 1400°K, *Phys. Rev.* 130 (1963) 1743–1748, <https://doi.org/10.1103/PhysRev.130.1743>.
- [34] C.J. Glassbrenner, G.A. Slack, Thermal conductivity of Si and Ge from 3 K to the melting point, *Phys. Rev.* 134 (1964) 1058–1069.
- [35] L. Thumfart, *Thermal Characterization of Si/Ge, InAs/GaAs Superlattice Structures, and AlGaN Films*, University Linz, 2020.
- [36] Q. Wang, J. Chang, H.P. Wang, Thermophysical properties and atomic structure of liquid Si-Ge alloys, *Mater. Chem. Phys.* 221 (2019) 224–231, <https://doi.org/10.1016/j.matchemphys.2018.09.043>.
- [37] E. Yamasue, M. Susa, H. Fukuyama, K. Nagata, Thermal conductivities of silicon and germanium in solid and liquid states measured by non-stationary hot wire method with silica coated probe, *J. Cryst. Growth* 234 (2002) 121–131.
- [38] Q. Zhang, Y. Liu, J. Yan, C. Zhang, Y. Hao, G. Han, Theoretical investigation of tensile strained GeSn waveguide with Si₃N₄ liner stressor for mid-infrared detector and modulator applications, *Opt. Exp.* 23 (2015) 7924, <https://doi.org/10.1364/OE.23.007924>.
- [39] M. Kurosawa, Y. Tojo, R. Matsumura, T. Sadoh, M. Miyao, Single-crystalline laterally graded GeSn on insulator structures by segregation controlled rapid-melting growth, *Appl. Phys. Lett.* 101 (2012) 091905, <https://doi.org/10.1063/1.4748328>.
- [40] L. Kormoš, M. Kratzer, K. Kosteckí, M. Oehme, T. Šíkola, E. Kasper, et al., Surface analysis of epitaxially grown GeSn alloys with Sn contents between 15% and 18%, *Surf. Interface Anal.* 49 (2017) 297–302, <https://doi.org/10.1002/sia.6134>.